Explosive shock processing of $Pr_2Fe_{14}B/\alpha$–Fe exchange-coupled nanocomposite bulk magnets

Z.Q. Jin
School of Materials Science and Engineering, Georgia Institute of Technology, Atlanta, Georgia 30332; and Department of Physics, University of Texas at Arlington, Arlington, Texas 76019

N.N. Thadhani,[a)] M. McGill, Y. Ding, and Z.L. Wang
School of Materials Science and Engineering, Georgia Institute of Technology, Atlanta, Georgia 30332

M. Chen and H. Zeng
IBM T.J. Watson Research Center, Yorktown Heights, New York 10598; and Department of Physics, University of Texas at Arlington, Arlington, Texas 76019

V.M. Chakka and J.P. Liu
Department of Physics, University of Texas at Arlington, Arlington, Texas 76019

Explosive shock compaction was used to consolidate powders obtained from melt-spun $Pr_2Fe_{14}B/\alpha$–Fe nanocomposite ribbons, to produce fully dense cylindrical compacts of 17–41-mm diameter and 120-mm length. Characterization of the compacts revealed refinement of the nanocomposite structure, with approximately 15 nm uniformly sized grains. The compact produced at a shock pressure of approximately 1 GPa maintained a high coercivity, and its remanent magnetization and maximum energy product were measured to be 0.98 T and 142 kJ/m^3, respectively. The compact produced at 4–7 GPa showed a decrease in magnetic properties while that made at 12 GPa showed a magnetic softening behavior. However, in both of these cases, a smooth hysteresis loop implying exchange coupling and a coercivity of 533 kA/m were fully recovered after heat treatment. The results illustrate that the explosive compaction followed by post-shock heat treatment can be used to fabricate exchange-coupled nanocomposite bulk magnets with optimized magnetic properties.

I. INTRODUCTION

A variety of nanocomposites consisting of hard magnetic $R_2Fe_{14}B$ (R = rare earth) and soft magnetic α–Fe or Fe_3B phases are being extensively investigated due to their potentially higher maximum energy product $(BH)_{max}$ through the exchange coupling between neighboring magnetic phases.[1,2] The prerequisite for effective exchange coupling is a small grain size of soft magnetic phase,[1] with the critical dimension estimated to be less than the twice domain wall width of the hard magnetic phase,[3] which is usually in the order of 10 nm. Nanocomposites with such characteristics have been recently shown to have significantly improved magnetic properties.[4–8] However, these nanocomposites have been typically produced in the form of powders or thin films, and there exist major obstacles in producing bulk nanocomposite magnets. Conventional sintering and hot-pressing methods, which are usually used to produce single-phase microcrystalline permanent magnets, are not favored in making bulk nanocomposite magnets because it is difficult to avoid grain growth during these processes. Nanocrystalline bulk magnets have also been produced by resin bonding. However, resin-bonded magnets generally suffer from a loss in remanence. Hence, there exists a need to develop a method that can produce monoliths from powders without changing their unique ultrafine grain (nanoscale) structure.

Dynamic shock compaction of powders has been successfully used as a powder consolidation technique for making bulk nanocrystalline and metastable materials[9–12] for which long-term thermal exposures would be undesirable. Shock compaction is a one-stage densification/bonding process that involves consolidation of powders via the intense deposition of shock energy at inter-particle regions resulting in localized deformation and plastic flow of surfaces in the process of void annihilation. Large amounts of plastic deformation, particle fracture, and grain size reduction, can also occur in the process of void collapse as the powders are compacted to full density. The consolidation pressures are typically in

the order of a few to tens of giga-Pascals and the duration of the pressure pulse is up to a few microseconds, depending on the consolidation geometry (gas gun or explosive loading) used. Consolidation of powders utilizing shock waves has been successfully used to prepare fully dense compacts of metals, alloys, and ceramics, while retaining the structural characteristics of the starting materials.[13]

Shock waves can be generated by the impact of a projectile accelerated using a gas gun or explosive loading devices or by detonating explosive charges in contact with the powder container. The gas-gun loading technique is generally used for making small-scale bulk materials to study the effects of compact characteristics as a function of more controlled shock-compression conditions, while explosive compaction is more amenable to the production of large-scale samples. Explosive compaction also has the potential of being effectively used for low-cost, high-volume production of bulk compacts of nanomaterials. Considerable work has been performed in characterizing the microstructural and magnetic properties of explosively compacted single-phase RFeB[9,14] and SmFeN alloys.[15] Preparation of bulk $Nd_2Fe_{14}B/Fe_3B$ nanocomposite magnets by dynamic compaction (using a propellant gun facility) has also been reported by Saito.[12] However, the compact had low coercivity ($H_c \sim$ 215 kA/m) and its density was only approximately 85% of the ingot density. Recently, we investigated the shock consolidation of $Pr_2Fe_{14}B/\alpha$–Fe nanocomposite powders using a 3-capsule plate-impact gas gun recovery fixture with shock loading conditions and capsule geometry designed based on two-dimensional computer simulations of shock wave propagation characteristics. A significant advantage of using Pr rather than Nd in the RFeB systems is its larger magnetocrystalline anisotropy constant, which is apparently beneficial to procurement of a higher intrinsic coercivity. Moreover, the $Pr_2Fe_{14}B$ magnets do not show spin reorientation transformation below the room temperature, making them potential for the applications at low temperature. Fully dense bulk $Pr_2Fe_{14}B/\alpha$–Fe nanocomposite magnets were successfully produced, while retaining the nano-scale structure and magnetic properties with H_c of 516 kA/m and $(BH)_{max}$ of 128 kJ/m^3.[16,17] These results provide the rationale that dynamic shock compaction can be used for preparation of bulk nanostructured magnets by optimization of compaction parameters by proper design of fixtures and use of powder morphology that allows for high initial packing density. To determine that scale-up of the dynamic shock compaction process is possible while retaining and even possibly further improving the magnetic properties, we investigated explosive shock compaction of $Pr_2Fe_{14}B/\alpha$–Fe nanocomposite powders using a double-tube cylindrical-implosion geometry. This configuration allows a radial build-up of pressure within the powder

assembly rather than a planer-wave propagation in the plate-impact experiments using a gas gun.[16] In this paper, the explosive compaction conditions determined using two dimensional numerical simulations was first discussed. The cylindrical isotropic bulk compacts of 17–41 mm diameter and 120 mm length was produced. The microstructure and magnetic properties of these compacts were characterized as a function of consolidation conditions as well as their variability in a given compact based on correlations with predictions from numerical simulations.

II. EXPERIMENTAL PROCEDURE

Melt-spun $Pr_2Fe_{14}B$ based nanocomposite ribbons, with 20 wt% α–Fe, were used in this study. The ribbons were ground into powder flakes having a size of 10–200 μm and packed in a steel container tube at ~60% theoretical mass density (TMD). The experimental configuration, shown schematically in Fig. 1, used a cylindrical implosion geometry consisting of two concentric tubes of approximately 152 mm length, with the internal
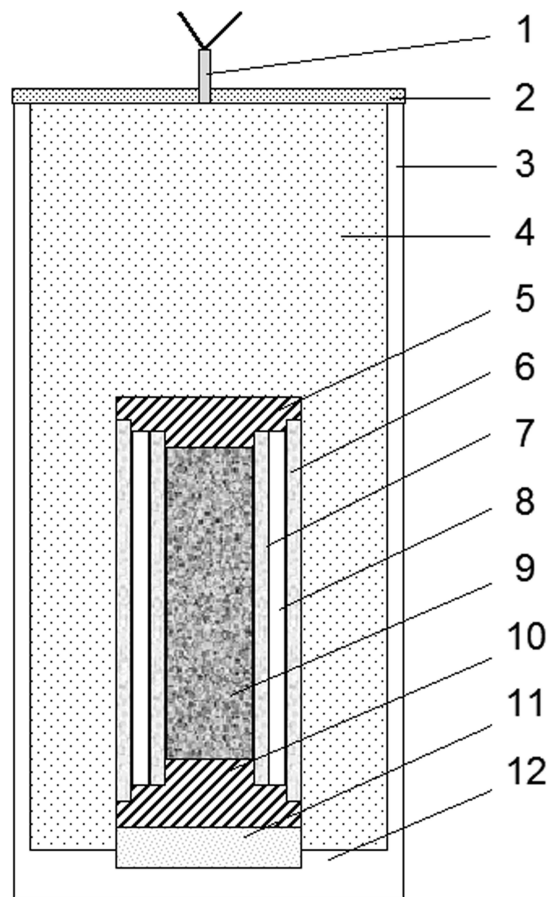

FIG. 1. Schematic view of explosive compaction setup: (1) detonator, (2) datasheet booster, (3) PVC pipe, (4) explosive, (5) steel top plug, (6) flyer tube, (7) powder container, (8) void, (9) nanocomposite powder, (10) steel bottom plug (11) momentum trap, (12) wood base.

steel tube containing the powder and the external steel tube acting as the flyer tube, which accelerated inwards upon detonation of the surrounding explosive. Steel plugs were used to seal the container at opposite ends. The assembly was placed concentrically in a polyvinyl chloride (PVC) pipe approximately 152 mm in diameter and surrounded with ammonium nitrate and fuel oil mixed with low density perlite diluent (ANFOIL) explosive. As shown in the figure, the length (304 mm) of the explosive-containing PVC pipe was taken to be equal to the length of the steel tube with top and bottom plugs, plus the PVC pipe diameter, which allowed planar-wave propagation through the explosive prior to its reaching the concentric steel tube assembly. A datasheet booster was placed on top of the explosive in contact with the detonator to generate a shock wave and initiate the ANFOIL explosive. Upon initiation, the detonation wave sweeps along the flyer tube and accelerates it inward, resulting in a convergent shock wave propagating through the length of the cylinder, and subsequently resulting in powder compaction. The detonation pressure P_d of the ANFOIL explosive can be altered by varying the concentration of the low-density perlite additive, thereby influencing the flyer tube implosion velocity; consequently the shock pressure propagates through and consolidates the powder. Shock compaction pressure P_s can also be altered by varying the diameter and wall thickness of the two concentric tubes. In the present work, two types of geometries and explosive-diluent concentrations were used. The first (referred to as COMP-A) used a flyer tube with a small inner diameter of 39 mm and explosive ANFOIL containing 14 wt% perlite. The second (referred to as COMP-B) used a flyer tube with a larger inner diameter of 69 mm, and ANFOIL containing 20 wt% perlite. The wall thickness of the respective container and flyer tubes was similar in both cases.

Following shock compression, the compacts were recovered in the form of cylinders of approximately 120-mm length and approximately 17-mm diameter for COMP-A and 41-mm diameter for COMP-B. The densities of these compacts were determined using the Archimedean method, and microhardness measurements were performed using the LECO DM-400F (St. Joseph, MI) microhardness tester to evaluate the mechanical integrity of the consolidated powder compacts. The starting powders and the recovered shock-consolidated compacts were characterized by x-ray diffraction (XRD) using Cu K$_\alpha$ radiation (λ = 1.54 Å), scanning electron microscopy (SEM), and transmission electron microscopy (TEM). Differential thermal analysis (DTA) was performed using a Perkin-Elmer DTA7 (Wellesley, MA) at a heating rate of 20 K/min to check for structural changes caused by post-shock heat treatments. The magnetic properties were measured using a superconducting quantum interference device magnetometer with a maximum applied

field of 5570 kA/m. The measured magnetic properties were corrected by using effective demagnetization factor (estimated according to the sample morphology) of 0.33 and 0.14 for starting powders and shock compacted samples, respectively.

III. RESULTS AND DISCUSSION

A. Calculation of shock compaction pressure for double-tube implosion system

The double tube cylindrical implosion system involves the implosion of a flyer tube onto a powder container generating a shock wave propagating through and consolidating the powder. The shock pressure acting on the powders is directly related to the implosion velocity of flyer tube, which can be estimated (based on the geometry used) as described by Meyers and Wang using the Gurney equation (see Ref. 18)

$$V_p = \sqrt{2E}$$

$$\left(3 \left/ \left[5(m_1/m_2) + 2(m_1/m_2)\frac{2R+r}{r} + \frac{2r}{R+r} \right] \right. \right)^{1/2} ,$$

where, $\sqrt{2E}$ (selected to be 0.7 km/s) reflects the Gurney energy of explosive charge, R and r are the inner diameter of the explosive container and flyer tube, respectively, and m_1/m_2 is the ratio between the mass of the flyer tube and the mass of the explosive, which can be expressed by

$$m_1/m_2 = \frac{\rho_1}{\rho_2}\left[\frac{(r+t)^2 - r^2}{R^2 - (r+t)^2} \right] ,$$

where ρ_1 and ρ_2 are the densities of flyer tube and the explosive, respectively, and t is the thickness of flyer tube. For a selected size R (~152 mm) of explosive container and thickness t (~5 mm) of flyer tube, increasing the size of the flyer tube r results in variation of m_1/m_2 and thus, the flyer tube implosion velocity. With increase in the diameter of the flyer tube from 39 to 69 mm, the resulting flyer tube implosion velocity decreases from 380 to 290 m/s. Since the shock pressure acting on the powders varies with the square of the impact velocity,[18] the shock pressure at the interface between flyer tube and powder decreases correspondingly.

For the shock compaction of powders, the consolidation history within the powder assembly is more complicated. Involving the variations in the thickness of flyer tube and the difference in $\sqrt{2E}$ and density ρ_2 due to different explosive diluent concentrations (14 and 20 wt% perlite for COMP-A and COMP-B, respectively), the corresponding maximum peak shock pressures generated in the powders were thus calculated, using the AUTODYN-2D computer code[19] and the P–α

J. Mater. Res., Vol. 20, No. 3, Mar 2005

601

model of powder densification.[20] Figures 2(a) and 2(b) show the collapse of the flyer tube onto the inner powder container tube, and propagation of the initial shock wave down the concentric tube assembly resulting in the radial build-up of pressure along the compact axis. It can be seen that peak pressure generated varies such that it is highest along the axial core, and it decreases to a more uniform pressure along the bulk of the outer regions. The initial compaction pressure was thus, calculated to be in the range of 4–7 GPa and 0.6–1 GPa for COMP-A and COMP-B, respectively. As the shock wave reaches the bottom steel plug [Fig. 2(c)], a build up of pressure is observed due to radial wave interaction, which results in a higher pressure shock wave (~12 GPa for COMP-A) entering from the bottom and concentrating along the compact axis as a Mach stem (region of high pressure and high temperature).

B. Physical characteristics of explosively compacted samples

Following explosive shock consolidation, cylindrically shaped compacts of nanocomposite magnets were obtained as shown in the photograph of a recovered compact in Fig. 3. It can be seen that except for the top and bottom plug regions (which are around ~1/8 length of the cylinder from the top and bottom surface, respectively), the cylinder has been subjected to uniform deformation throughout its length. This is consistent with AUTODYN-2D simulation results shown earlier in Fig. 2. The top view of the compacted samples shows spoke-like radial lines, revealing the geometrical effect of the convergence of axisymmetric shock waves.

Figures 4(a) and 4(b) show photographs of cross sections of the top and bottom regions of COMP-A (4–7 GPa shock pressure) compact, respectively. For the top
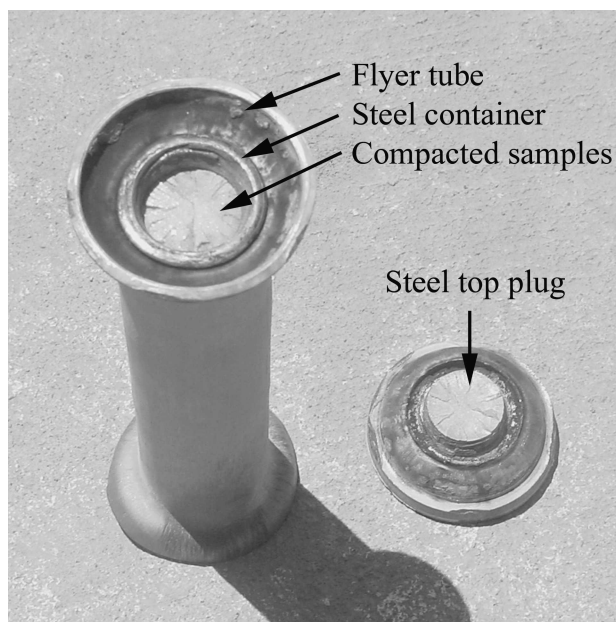

FIG. 3. Photograph of the cylinders after explosive compaction.

region [Fig. 4(a)], the original steel tube of 22 mm diameter has been constricted down to 17 mm, resulting in 23% deformation and consequent densification of the nanocomposite powders. The density of the axial region of the compact along its mid-length is around 98.5% TMD, while that of the outer regions is 97–98% TMD. The higher density in the center region can also be illustrated by its more condensed surface morphology. In the photograph, macrocracks generated due to tension from radial release waves are also observed. The bottom section of the compact shows an axial cavity [Fig. 4(b)], which is attributed to an effect of a Mach stem. The Mach stem originated from the convergence of a high-pressure shock wave along the cylinder axis generated in
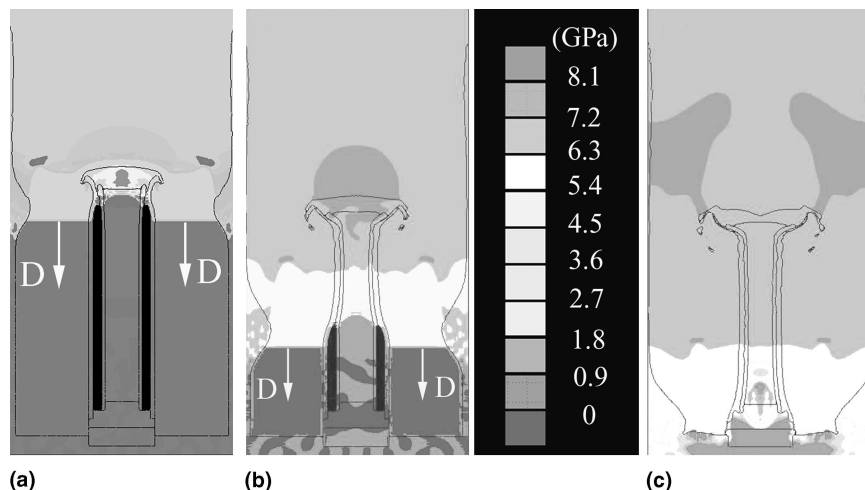

FIG. 2. AUTODYN-2D model of double-tube explosive compaction showing pressure contour at (a) 80 μs, (b) 128 μs, (c) 166 μs.
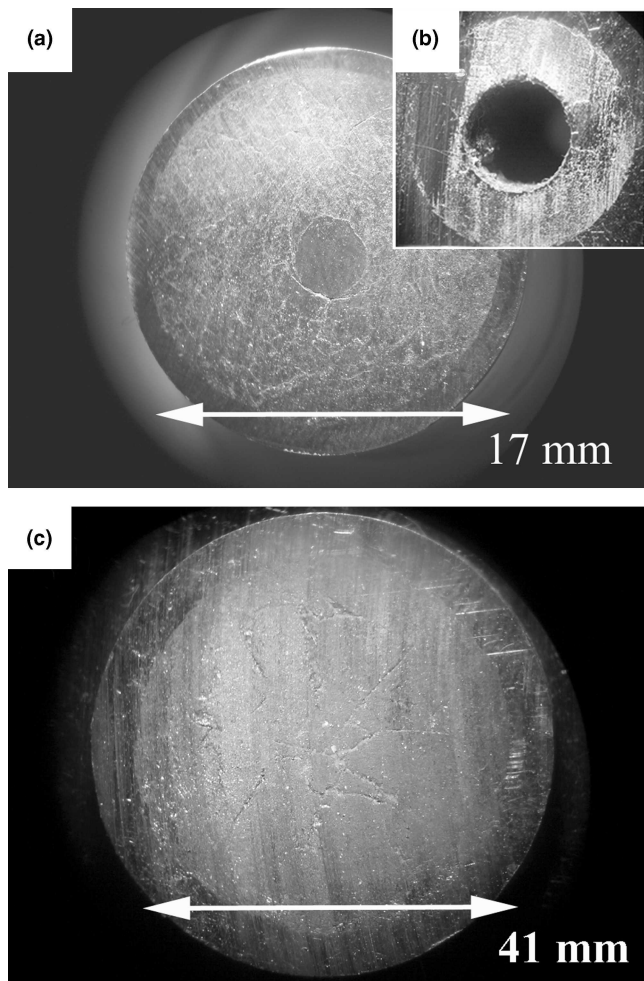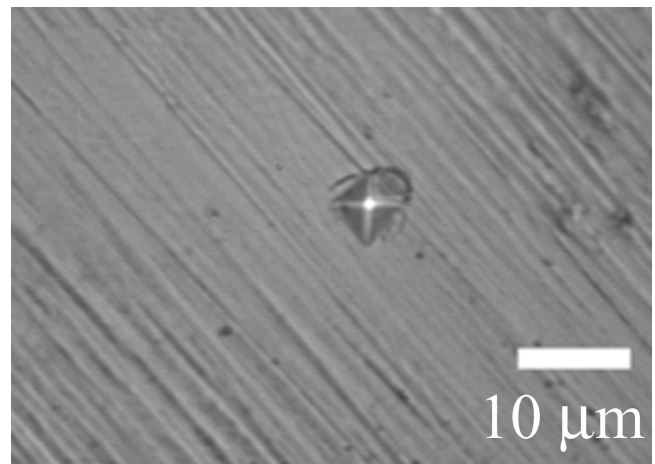
FIG. 4. Cross section of regions located nearby (a) top and (b) bottom of COMP-A; (c) cross section of COMP-B.

the bottom part of the compact as described earlier. The cavity with a maximum diameter of approximately 10 mm extends to almost three-quarters of the length of the cylindrical compact. The inner surface of the cavity shows evidence of formation of traces of melted and resolidified material. Similar formation of melted and resolidified regions in the Mach stem has also been observed in single-tube explosively compacted NdFeB magnets.[9] Formation of the Mach stem and resulting cavity can be eliminated by reducing the detonation pressure of explosive or by increasing the diameter of double-tube assembly to dissipate the shock pressure more effectively.
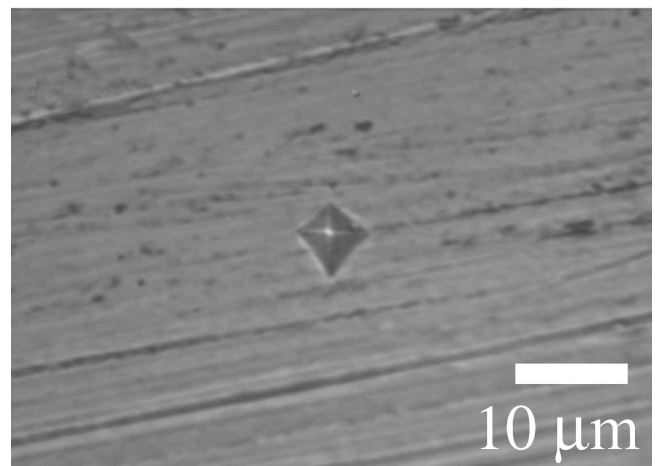
Consistent with the results of AUTODYN-2D computer simulations, the COMP-B sample subjected to shock pressure of 0.6–1 GPA (substantially lower than 4–7 GPa pressure in COMP-A) shows a more uniform densification without the deep cavity [Fig. 4(c)]. The original steel container of 51 mm in diameter was constricted down to 41 mm resulting in approximately 20%

deformation (which is slightly lower than that in COMP-A) and a uniform compact density of 97–98% TMD maintained throughout the length of the compact. The overall degree of densification was quite similar to that observed in our previous work on shock-consolidated samples prepared using the gas gun.[16]

The measured average Vickers microhardness of the shock compressed samples is approximately 11 GPa, which is again similar to that measured on our gas-gun compacted samples.[16] Figure 5 shows images of typical hardness indentations in an unpolished COMP-A sample. For the top region (4–7 GPa medium pressure region), the cracks emanating from the tips of the indentation are observed, indicating the intrinsic brittleness of the melt-spun and shock compacted PrFeB alloy compact. This characteristic is also observed for the COMP-B sample. For the bottom region (12 GPa high pressure region), no emanated cracks are observed, indicating a better cohesion.

FIG. 5. Microphotographs of (a) top and (b) bottom region of COMP-A showing typical hardness indentation in the compacted samples.

C. Microstructural characteristics of compacts

Figure 6 compares the XRD patterns of starting powder materials, explosively consolidated samples, and heat-treated samples following shock consolidation. It can be seen that the original nanocomposite structure (mixture of hard 2:14:1 phase and soft $\alpha-Fe$) is retained upon explosive compaction as revealed by traces b (COMP-B) and d (COMP-A). However, the shock-compressed sample shows broadened peaks, which is more evident for the high-pressure compact (COMP-A) as seen from trace d. Broadening of x-ray diffraction peaks has also been observed in $SmCo_5$ magnets shocked compacted at moderate pressures,[21] and been correlated to grain refinement or the existence of retained plastic strain.[16] In our case, the shock induced strain was found to be around 0.3–0.5% calculated using the Williamson–Hall method based on the peak broadening in comparison with nearly-zero strain value of starting materials. Annealing of the shock consolidated compacts at 750 °C for 3 min does not significantly change the microstructure except for narrowing of the diffraction peaks (as shown by traces c and e in Fig. 6) due to strain relaxation and/or a slight grain growth, as revealed by TEM analysis (shown in Sec. III. D).

Figure 7 shows results of DTA analysis performed on the as-received and the two shock-consolidated samples

FIG. 7. DTA analysis on the (a) starting materials, (b) COMP-A, and (c) COMP-B.

COMP-A and COMP-B. While the starting ribbon powder trace [Fig. 7(a)] shows no thermal activity except for endothermic peaks indicating melting of hard-phase $Pr_2Fe_{14}B$ and soft-phase iron, a small exothermic bump is visible around 620 °C (as marked by the arrow) in the two shock compacted samples. The exothermic temperature is very close to the crystallization temperature of 2:14:1 amorphous phase.[22] It is believed that the crystallization event observed in the DTA traces of the shock-consolidated samples corresponds to the amorphous phase formed during the shock compaction process, although its presence was not detected in XRD patterns.

Figures 8(a) and 8(b) show the typical scanning electron microscope (SEM) micrographs for COMP-A and COMP-B. It can be seen that the individual flaky powders are substantially compressed and deformed to fill the interstices, thereby resulting in an irrevocably altered configuration produced due to explosive shock compaction. Both compacts are found to undergo nearly complete consolidation as revealed by intimate bonding between the particles and absence of any interparticle cracking/separation. However, some transparticle macrocracks are also observed [Fig. 8(b)] in the samples and are believed to have been formed due to radial loading and release wave interactions.

During shock compression, the deformation and densification energy is converted to thermal energy, which can significantly increase the mean-bulk (residual) temperature. However, due to rapid densification achieved
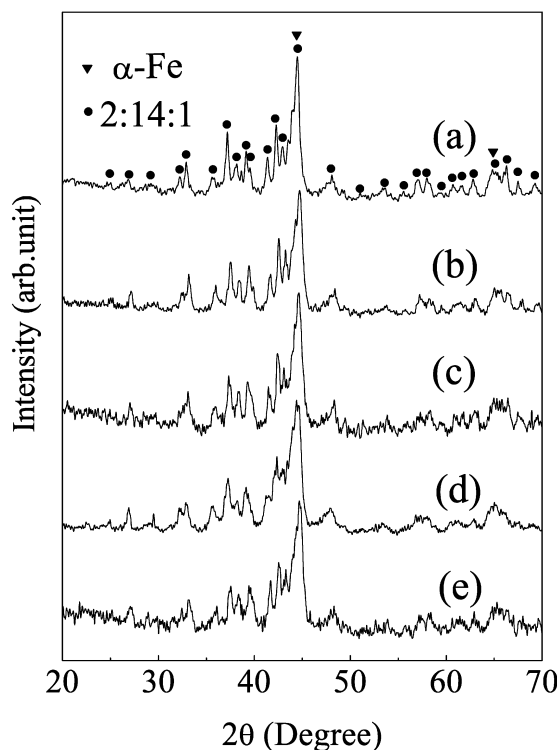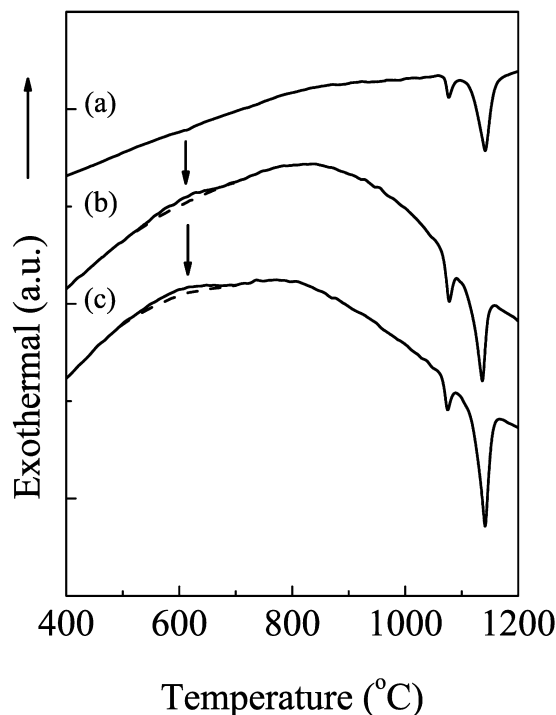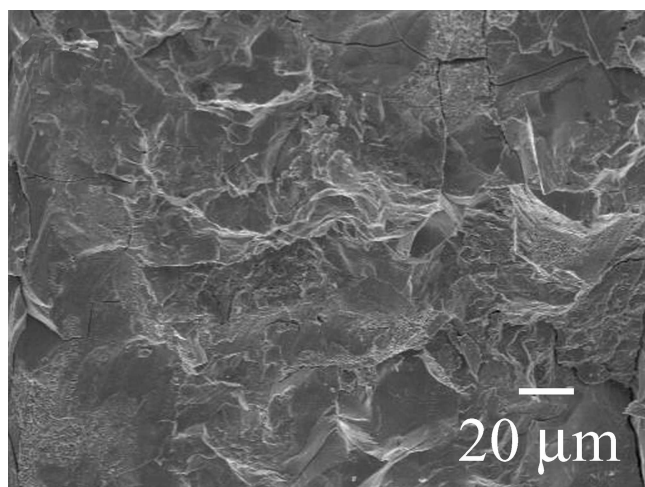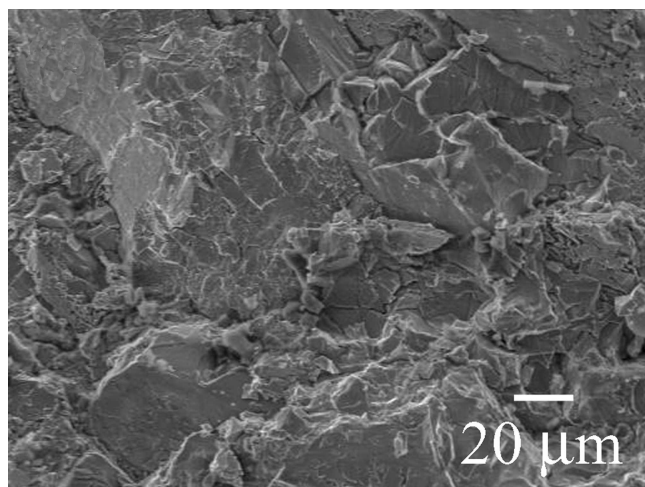
FIG. 6 X-ray diffraction patterns of (a) starting materials, (b) as-compacted, and (c) annealed COMP-B; (d) as-compacted, and (e) annealed COMP-A. The annealing temperature is 700 °C.

(a)

(b)

FIG. 8. SEM image of (a) fracture surface of COMP-A, (b) enlarged image of localized regions in COMP-A showing deformation, (c) fracture surface of COMP-B, and (d) enlarged image of localized regions in COMP-B showing deformation.

by the passage of shock waves of sufficient magnitude within time duration of microseconds followed by the rapid heat dissipation rates of 10^9 K/s,[21] thermally induced microstructural changes and grain growth can be minimized. The effect of shock compaction on interparticle morphology was studied in detail using TEM analysis performed on top and bottom regions of the as-compacted and annealed samples of COMP-B. As shown in Fig. 9, a very fine microstructure with grain size around 10–15 nm and 15–20 nm was observed for the top [Fig. 9(a)] and bottom [Fig. 9(b)] regions of the compact, respectively. Furthermore, the grain size was observed to be quite homogeneous. The retention of a stable ultrafine grain size is an important characteristic of the shock compaction process. In fact, even upon annealing the shock consolidated samples at a temperature of approximately 750 °C for 3 min, little grain growth was

observed as shown in Figs. 9(c) and 9(d), with most grains being 15–20 nm in size, although some grains 25 nm in size are also present. The retention of nanoscale grain size provides the possibility of optimal magnetic properties through exchange coupling between the hard magnetic $Pr_2Fe_{14}B$ and soft magnetic α–Fe phases. High-resolution TEM (HRTEM) [Fig. 10(a)] shows that the fine nanoscale morphology of magnetic nanocomposites consists of multiple magnetic phases. The presence of an amorphous phase is also clearly evident in the shock compacted samples, consistent with the results of DTA analysis indicating presence of a small exotherm corresponding to crystallization of amorphous phase (Fig. 7). HRTEM analysis of the annealed shock-consolidated sample shows no presence of the amorphous phase indicating its crystallization into $Pr_2Fe_{14}B$ and α–Fe phases upon heat treatment [Fig. 10(b)].

Shock compression of brittle materials at pressures exceeding the Hugoniot-elastic limit generally introduces defects such as macro-and micro-cracks, dislocations, twinning, phase transformation, and even shear banding in compacts of microcrystalline powders.[23–25] In the present work on explosively shock compacted samples, HRTEM analysis confirmed the presence of defects in the form of twinning and dislocations within $Pr_2Fe_{14}B$ grains. Figures 11(a) and 11(b) show HRTEM images of these structural defects, most preferentially observed in $Pr_2Fe_{14}B$ grains, but are limited in extent and number. Formation of shear banding has also been observed in our previous work on the gas-gun compaction of $Pr_2Fe_{14}B/$ α–Fe nanocomposite magnets.[26]

D. Magnetic properties of compacts

The magnetic properties were measured on small samples of several cubic millimeters, sectioned from various regions of the shock-consolidated compacts. Figure 12 shows the hysteresis loops of different regions of shock compacted samples COMP-A and COMP-B. Both the top and bottom regions of the low-pressure shock consolidated COMP-B samples show smooth hysteresis loops with larger coercivity H_c and remanence M_r as shown in Figs. 12(a) and 12(b). The best magnetic properties with remanence M_r of 0.98 T, coercivity H_c of 533 kA/m, and maximum energy product $(BH)_{max}$ of 142 kJ/m^3, were obtained in the area near the bottom region of the COMP-B sample. Consistent magnetic properties of H_c around 509–533 kA/m and $(BH)_{max}$ around 119–131 kJ/m^3 are also obtained through the mid-length regions of the cylindrical samples. The maximum energy products measured are superior than those of commercially available resin-bonded nanocomposites (96 kJ/m^3) in which nonmagnetic resins result in not only the decrease of density (<80% TMD) but also the reduction of magnetization and thereby the degradation of magnetic properties. Of more importance is the fact that
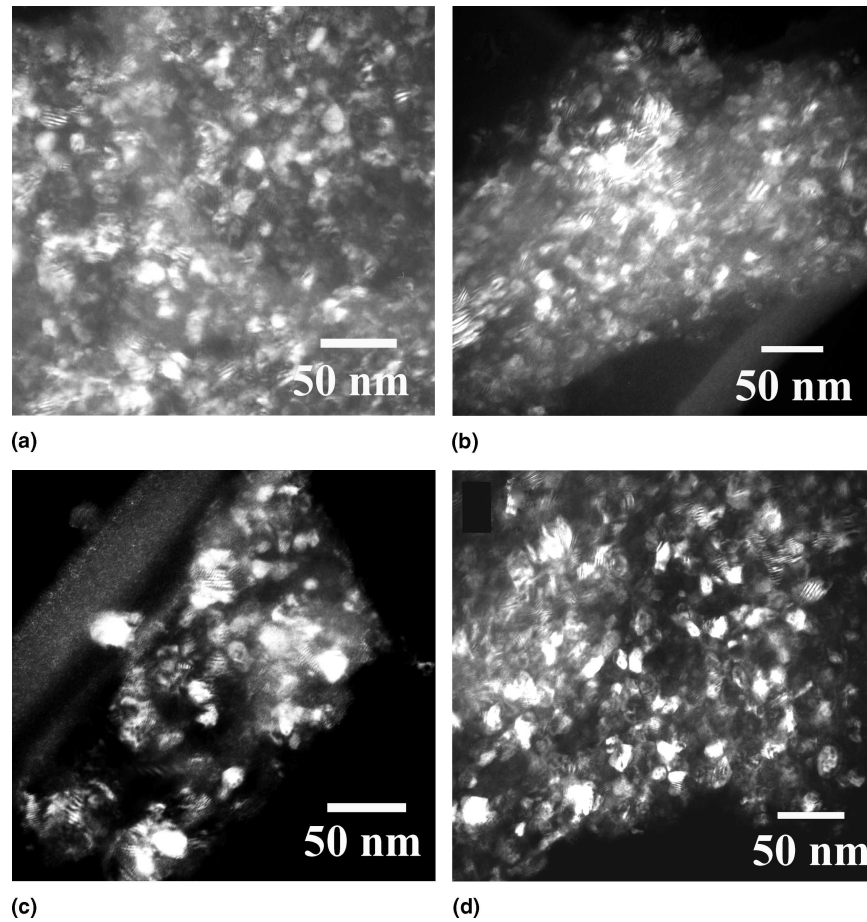
FIG. 9. TEM images of (a) top and (b) bottom region of as-compacted COMP-B, (c) top and (d) bottom region of COMP-B annealed at 700 °C for 3 min.

the optimal magnetic properties are closely associated with the retention of nanostructure and strong exchange coupling between hard and soft magnetic phases. It is well known that for optimum exchange coupling, the size of the soft magnetic α–Fe grains should be approximately twice that of the effective exchange range L_{ex}.[27,28] A larger grain size above $2L_{ex}$ results in hysteresis loops of contracted shape, and corresponding deterioration of magnetic properties. The optimum grain size $2L_{ex}$ has been found to be around 15 nm in $Nd_2Fe_{14}B/$ α–Fe nanocomposites, which is very similar to the grain size of α–Fe phase observed via HRTEM analysis of the shock-compacted samples. The present results thus illustrate that the optimum magnetic properties are obtained in as-compacted sample by proper control of the shock compaction pressure. Further grain refinement would be expected to provide more significant improvement in magnetic properties.

The high-pressure (4–7 GPa) compact COMP-A shows a low coercivity for the top region [Fig. 12(c)] and even a complete magnetic softening behavior for the bottom region [Fig. 12(d)] where a calculated pressure of 12 GPa occurs as result of reflections from the bottom

plug. The shock pressure is actually lower than the 28–38 GPa pressure required for complete demagnetization of $Nd_2Fe_{14}B$ magnets occurring via ferromagnetic-to-paramagnetic phase transformation due to high velocity impact.[23,29]
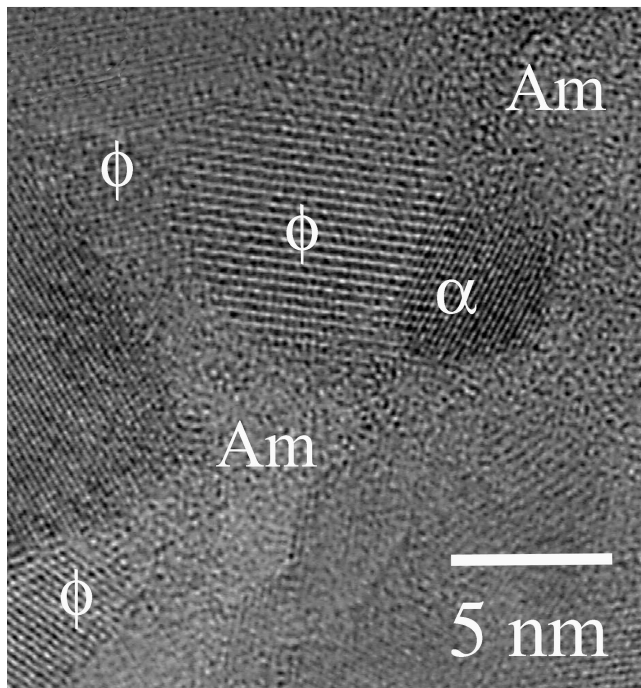
The magnetic softening behavior of the COMP-A sample can be explained in terms of the magnetization reversal mechanism of nanocomposites.[30] The coercivity H_c of nanocomposite is usually related to nucleation field H_n, which can be expressed as
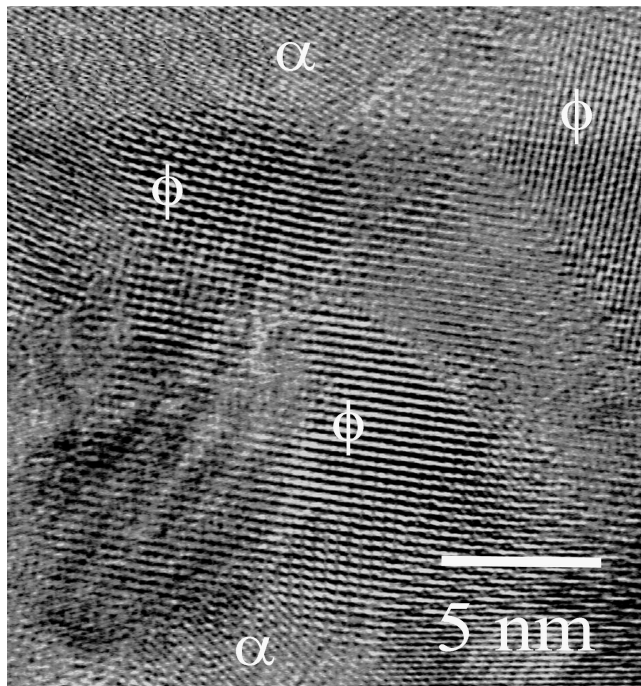
$$H_c = \alpha H_n - N_{eff}M_s \quad .[31]$$

In this expression, α and N_{eff} are microstructure-dependent parameters, M_s is the saturation magnetization, and

$$H_n = 2[f_sK_s + (1 - f_s)K_h]/\mu_0M_s$$

where f_s *is* volume fraction of soft phases (α–Fe plus amorphous soft phases in our cases), and K_h and K_s are anisotropy constants of hard and soft phases, respectively. Previous calculation has shown that the anisotropy constants K_h and K_s decrease with the reduction of grain sizes of both hard and soft magnetic phases.[32] The grain
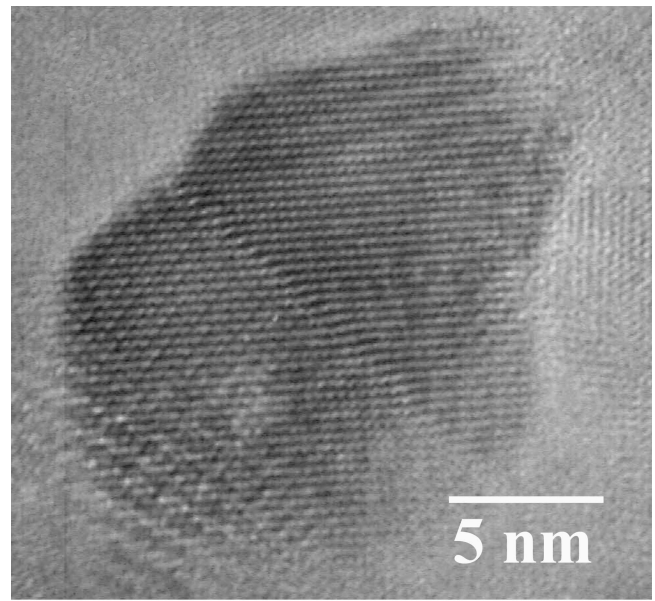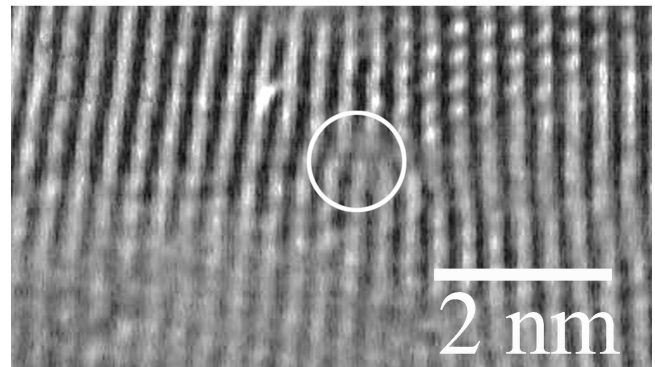
(a)

(b)

FIG. 10. HRTEM images of (a) as-compacted and (b) annealed COMP-B. ϕ, α, and AM denote $Pr_2Fe_{14}B$, α–Fe and amorphous phases, respectively.

refinement has been confirmed by XRD and TEM observation in our work. This grain refinement apparently leads to the increase of number of reversal nucleation centers at grain boundary, which may result in a lowered reversal field. Anisotropy constants are also associated

(a)

(b)

FIG. 11. HRTEM of COMP-B showing the (a) twinning structure and (b) dislocation in $Pr_2Fe_{14}B$ crystallites.
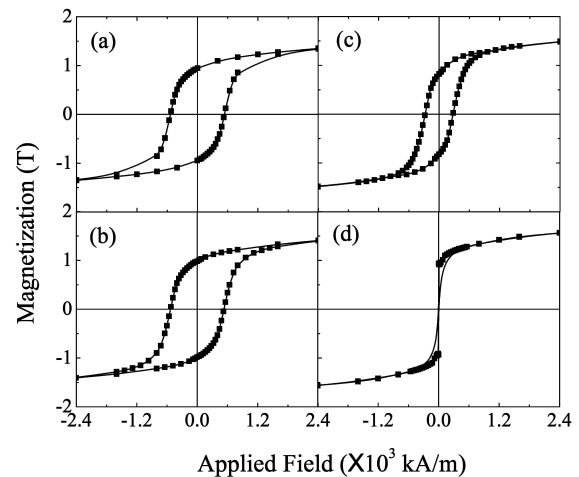

FIG. 12. Hysteresis loops of explosively compacted samples: (a) top and (b) bottom region of COMP-B, (c) top, and (d) bottom region of COMP-A.
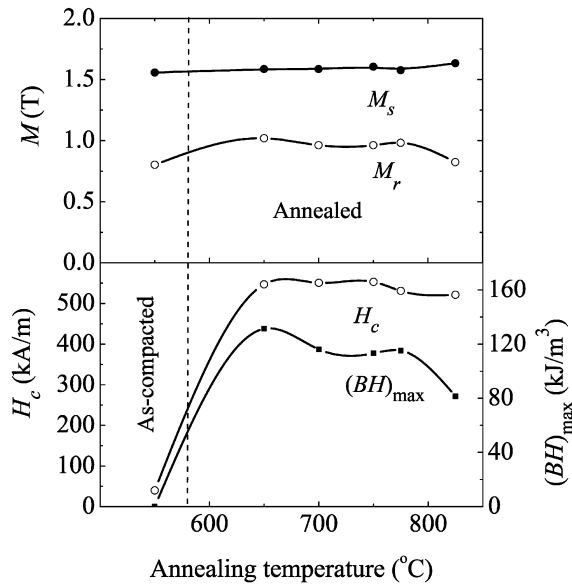
FIG. 13. The magnetic properties of bottom region of samples COMP-A annealed at different temperatures for 3 min.

FIG. 14. Comparison of hysteresis loops of COMP-B before and after heat treatment at 700 °C for 3 min.

with the crystal structure[33] and the site preference of the transition metal ions in the crystal lattice in some cases.[34] The structural defects, such as dislocation or planar defect (twinning) regions introduced by the shock wave, will lead to the local changes in anisotropy constants. However, it is still not quite clear how these defects affect the intrinsic magnetic properties of nanocomposites. For the nanocomposite compacts, the structure defects are limited in the extent and amount in the present work. Undoubtedly, more deliberate works are necessary to address this important issue so as to help with the further optimization of shock compaction parameters. Additionally, shock-induced amorphorization leads to the increase of soft phase fraction, and as pointed previously, the nucleation field H_n decreases monotonically with the increase of soft phase content.[30] It is believed that all these factors are responsible for the change in coercivity even the occurrence of zero value in the as-compacted sample COMP-A.

Post-shock heat treatments were used to investigate the effect of annealing temperature on magnetic properties of the compacted samples. Figure 13 shows the magnetic properties of a sample from the bottom region of an annealed COMP-A compact. The saturation magnetization M_s was extracted from the hysteresis loop measurements by plotting the curve of M versus $1/H^2$ and extrapolating the curve to infinite H. The saturation magnetization M_s is slightly higher in the annealed samples, which may be attributed to the crystallization of amorphous phase and precipitation of α–Fe having high magnetization. The coercivity H_c and maximum energy product $(BH)_{max}$ is also observed to increase up to 533 kA/m and 127 kJ/m^3, which is close to those values of as-compacted COMP-B samples. The increase of magnetic
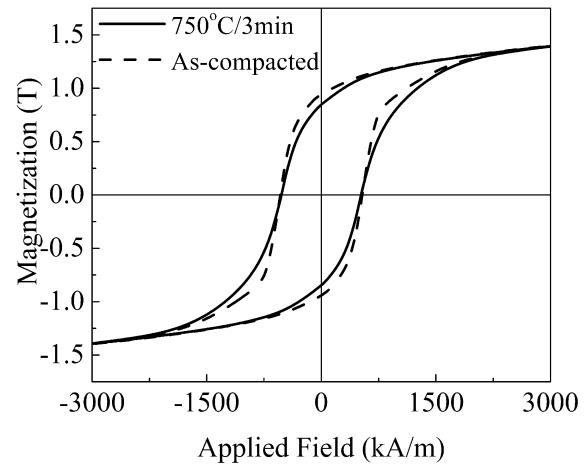
properties relates to the crystallization of amorphous phase in the explosively compacted samples and to the retention of nanostructure. Further increase in annealing temperature, however leads to the decrease of magnetic properties. The temperature dependence of $(BH)_{max}$ is same as the temperature dependence of M_r, revealing that the $(BH)_{max}$ is more sensitive to the remanence M_r rather than the coercivity H_c. The annealed sample of COMP-B shows slightly lower values of $(BH)_{max}$ (104–111 kJ/m^3) compared to as-compacted sample due to the decrease of remanence M_r with annealing treatment, although the coercivity does not change significantly as shown in Fig. 14. This implies that optimal magnetic properties can be directly obtained from the as-compacted samples by properly designation of the explosion parameters (such as explosive type and explosion compaction assembly size). The magnetic softening behavior of hard magnetic nanocomposites due to overloading of shock energy can be recovered by subsequent thermal treatment.

IV. SUMMARY

Explosive compaction has been shown to be an effective method to produce bulk nanocomposite magnets with nearly full density. Explosive compaction not only results in the extensive deformation and introduction of microstructural defects, like twinning and dislocation generation, but also the retention of the original nanostructure, and even a refinement of the grain size. The magnetic properties of bulk compacts are sensitive to shock pressure, which can be controlled by varying the shock compaction geometry (size of double-tube assembly and type of explosive used) and using numerical simulations to predict those desired shock-compaction conditions. The relatively lower pressure is better for the retention and even improvement of magnetic properties.

Although, magnetic properties have yet to be further improved, this study provides a step forward in illustrating that bulk nanocomposites with higher H_c and $(BH)_{max}$ than that of the starting powders can be fabricated by shock compaction.

ACKNOWLEDGMENT

REFERENCES

1. J. Wecker, K. Schnitzke, H. Cerva, and W. Grogger: Nanostructured Nd–Fe–B magnets with enhanced remanence. *App. Phys. Lett.* **67,** 563 (1995).

2. R. Coehoorn, D.B. de Mooij, J.P.W.B. Duchateau, and K.H.J. Buschow: Novel permanent magnetic-materials made by rapid quenching. *J. Phys. C* **49,** 669 (1988).

3. E.F. Kneller and R. Hawig: The exchange-spring magnet—A new material principle for permanent-magnets. *IEEE Trans. Magn.* **27,** 3588 (1991).

4. D. Goll, M. Seeger, and H. Kronmüller: Magnetic and microstructural properties of nanocrystalline exchange coupled PrFeB permanent magnets. *J. Magn. Magn. Mater.* **185,** 49 (1998).

5. Z.C. Wang, H.A. Davies, and C.L. Harland: Crystallization behavior and magnetic properties of melt-spun $Pr_x(Fe_{0.8}Co_{0.2})_{94-x}B_6$ alloys. *IEEE Trans. Magn.* **38,** 2967 (2002).

6. J.P. Liu, C.P. Luo, Y. Liu, and D.J. Sellmyer: High energy products in rapidly annealed nanoscale Fe/Pt multilayers. *Appl. Phys. Lett.* **72,** 483 (1998).

7. H. Zeng, J. Li, J.P. Liu, Z.L. Wang, and S.H. Sun: Exchange-coupled nanocomposite magnets by nanoparticles self-assembly. *Nature* **420,** 395 (2002).

8. Z.Q. Jin, B.Z. Cui, J.P. Liu, Y. Ding, Z.L. Wang, and N.N. Thadhani: Controlling the crystallization and magnetic properties of melt-spun $Pr_2Fe_{14}B/\alpha$–Fe nanocomposites. *Appl. Phys. Lett.* **84,** 4382 (2004).

9. S. Guruswamy, M.K. McCarter, J.E. Shield, and V. Panchanathan: Explosive compaction of magnequench Nd–Fe–B magnetic powders. *J. Appl. Phys.* **79,** 4851 (1996).

10. M. Leonowicz, W. Kaszuwara, E. Lezierska, D. Januszewski, G. Mendoza, H.A. Davies, and J. Paszula: Application of the shock compaction technique for consolidation of hard magnetic powders. *J. Appl. Phys.* **83,** 6634 (1998).

11. H. Oda, H. Hirai, K. Kondo, and T. Sato: Magnetic-properties of shock-compacted high-coercivity magnets with a nanometer-sized microstructure. *J. Appl. Phys.* **76,** 3381 (1994).

12. T. Saito: Production of bulk materials of an $Nd_4Fe_{77.5}B_{18.5}$ alloy and their magnetic properties. *IEEE Tran Magn.* **37,** 2561 (2001).

13. W.H. Gourdin: Dynamic consolidation of metal powders. *Prog. Mater. Sci.* **31,** 39 (1986).

14. S. Ando, Y. Mine, K. Takashima, S. Itoh, and H. Tonda: Explosive compaction of Nd-Fe-B powder. *J. Mater. Process. Technol.* **85,** 42 (1999).

15. T. Mashimo, X. Huang, S. Hirosawa, K. Makita, Y. Kato, S. Mitsudo, and M. Motokawa: Magnetic properties of fully dense $Sm_2Fe_{17}N_x$ magnets prepared by shock compression. *J. Magn. Magn. Mater.* **210,** 109 (2000).

16. Z.Q. Jin, K.H. Chen, J. Li, H. Zeng, S-F. Cheng, J.P. Liu, Z.L. Wang, and N.N. Thadhani: Shock compression response of magnetic nanocomposite powders. *Acta Mater.* **52,** 2147 (2004).

17. K.H. Chen, Z.Q. Jin, J. Li, G. Kennedy, Z.L. Wang, N.N. Thadhani, H. Zeng, S-F. Cheng, and J.P. Liu: Bulk nanocomposite magnets produced by dynamic shock compaction. *J. Appl. Phys.* **96,** 1276 (2004).

18. M.A. Meyers and S.L. Wang: An improved method for shock consolidation of powders. *Acta Metall.* **36,** 925 (1988).

19. AUTODYN-2D/2.8, Non-Linear dynamic modeling software (Century Dynamics Inc., Oakland, CA, 1995).

20. W. Hermann: Constitutive equation for the dynamic compaction of ductile porous materials. *J. Appl. Phys.* **40,** 2490 (1969).

21. R. Chau, M.B. Maple, and W.J. Nellis: Shock compaction of $SmCo_5$ particles. *J. Appl. Phys.* **79,** 9236 (1996).

22. Z.Q. Jin, H. Okumura, J.S. Muñoz, Y. Zhang, H.L. Wang, and G.C. Hadjipanayis: Multi-step crystallization evolution in nanocomposite $Pr_8Fe_{86}B_6$ alloys. *J. Phys. D: Appl. Phys.* **35,** 2893 (2002).

23. S.I. Shkuratov, E.F. Talantsev, J.C. Dickens, M. Kristiansen, and J. Baird: Longitudinal-shock-wave compression of $Nd_2Fe_{14}B$ high-energy hard ferromagnet: The pressure-induced magnetic phase transition. *Appl. Phys. Lett.* **82,** 1248 (2003).

24. M.A. Meyers: *Dynamic Behavior of Materials* (John Wiley & Sons, New York, 1994), p. 382.

25. N.N. Thadhani: Shock-induced and shock-assisted solid-state chemical-reactions in powder mixtures. *J. Appl. Phys.* **76,** 2129 (1994).

26. J. Li, Z.Q. Jin, J.P. Liu, Z.L. Wang, and N.N. Thadhani: Amorphization and ultrafine-scale recrystallization in shear bands formed in shock-consolidated $Pr_2Fe_{14}B/\alpha$–Fe nanocomposite magnets. *Appl. Phys. Lett.* **85,** 2223 (2004).

27. X.K. Sun, J. Zhang, Y.L. Chu, W. Liu, B.Z. Cui, and Z.D. Zhang: Dependence of magnetic properties on grain size of alpha-Fe in nanocomposite $(Nd,Dy)(Fe,Co,Nb,B)_{5.5}/\alpha$–Fe magnets. *Appl. Phys. Lett.* **74,** 1740 (1999).

28. H. Kronmüller, R. Fischer, M. Seeger, and A. Zern: Micromagnetism and microstructure of hard magnetic materials. *J. Phys. D: Appl. Phys.* **29,** 2274 (1996).

29. S.I. Shkuratov, E.F. Talantsev, J.C. Dickens, and M. Kristiansen: Transverse shock wave demagnetization of $Nd_2Fe_{14}B$ high-energy hard ferromagnetics. *J. Appl. Phys.* **92,** 159 (2003).

30. Z.H. Chen, J.X. Zhang, and H. Kronmüller: Magnetically soft phase in magnetization reversal processes of nanocomposite $Sm_2Fe_{15}Ga_2C_x/\alpha$–Fe permanent magnetic materials. *Phys. Rev. B* **68,** 144417 (2003).

31. J. Bauer, M. Seeger, A. Zern, and H. Kronmüller: Nanocrystalline FeNdB permanent magnets with enhanced remanence. *J. Appl. Phys.* **80,** 1667 (1996).

32. R.W. Gao, W.C. Feng, H.Q. Liu, B. Wang, W. Chen, G.B. Han, P. Zhang, H. Li, W. Li, Y.Q. Guo, W. Pan, X.M. Li, M.G. Zhu, and X. Li: Exchange-coupling interaction, effective anisotropy and coercivity in nanocomposite permanent materials. *J. App. Phys.* **94,** 664 (2003).

33. B.M. Moskowitz: Micromagnetic study of the influence of crystal defects on coercivity in magnetite. *J. Geophys. Res-Solid Earth.* **98,** 18011 (1993).

34. M.M. Abdelaal: Magnetic-behavior of $Y_2Fe_{14-x}T_xB$ compounds, where T = Al, Ti, V, Cr, Mn, Co or Ni. *J. Magn. Magn. Mater.* **131,** 148 (1994).